Continuum sea ice rheology determined from subcontinuum mechanics

Article

Published Version

Continuum sea ice rheology determined from subcontinuum mechanics

P. D. Taylor,[1] D. L. Feltham,[1,2] P. R. Sammonds,[3] and D. Hatton[3]

Received 8 April 2005; revised 25 July 2006; accepted 14 August 2006; published 25 November 2006.

[1] A method is presented to calculate the continuum-scale sea ice stress as an imposed, continuum-scale strain-rate is varied. The continuum-scale stress is calculated as the area-average of the stresses within the floes and leads in a region (the continuum element). The continuum-scale stress depends upon: the imposed strain rate; the subcontinuum scale, material rheology of sea ice; the chosen configuration of sea ice floes and leads; and a prescribed rule for determining the motion of the floes in response to the continuum-scale strain-rate. We calculated plastic yield curves and flow rules associated with subcontinuum scale, material sea ice rheologies with elliptic, linear and modified Coulombic elliptic plastic yield curves, and with square, diamond and irregular, convex polygon-shaped floes. For the case of a tiling of square floes, only for particular orientations of the leads have the principal axes of strain rate and calculated continuum-scale sea ice stress aligned, and these have been investigated analytically. The ensemble average of calculated sea ice stress for square floes with uniform orientation with respect to the principal axes of strain rate yielded alignment of average stress and strain-rate principal axes and an isotropic, continuum-scale sea ice rheology. We present a lemon-shaped yield curve with normal flow rule, derived from ensemble averages of sea ice stress, suitable for direct inclusion into the current generation of sea ice models. This continuum-scale sea ice rheology directly relates the size (strength) of the continuum-scale yield curve to the material compressive strength.

Citation: Taylor, P. D., D. L. Feltham, P. R. Sammonds, and D. Hatton (2006), Continuum sea ice rheology determined from subcontinuum mechanics, *J. Geophys. Res.*, *111*, C11015, doi:10.1029/2005JC002996.

1. Introduction

[2] Sea ice, frozen seawater, forms in the cold polar oceans of the Earth, may cover nearly 10% of the Earth's surface at its maximum extent, and plays an important role in both polar and global climate. In particular, by virtue of the high albedo of sea ice and snow-covered ice, variation in the area-coverage of sea ice has a significant impact on solar radiation absorbed by the ocean during summer. Sea ice is fresher than the ocean water from which it forms; the formation, movement and subsequent melt of sea ice constitutes a substantial thermohaline forcing on the ocean. The dense, salty water expelled during sea ice formation and aging is thought to play a significant role in deep water formation in both hemispheres.

[3] Global Climate Models (GCMs) typically contain relatively complex representations of the thermal and momentum balances of sea ice. The momentum balance for sea ice contains a representation of the sea ice forces, sometimes known as internal forces, that result from deformation of the ice cover, i.e. sliding of floes past each other, overriding and rafting of sea ice floes to form ridges, and formation of linear regions of open water known as leads (which quickly freeze over in winter). The relationship between these internal forces to the deformation of the ice cover and the properties of the ice cover is determined by the rheology of sea ice, which is usually considered to have a plastic character.

[4] GCMs use representations of sea ice rheology appropriate to their grid resolution. The grid resolution of GCMs is typically large enough, e.g. 100 km, that sea ice may be treated as a continuum and the sea ice rheology appropriate to this scale is representative of the average over the variety of ice types found in a region similar in size to a grid cell. The procedure by which a characteristic of sea ice at a point in a continuum model is related to the variety of values of this characteristic in the region over which the continuum assumption is invoked, e.g. the model grid cell, is known as homogenization. Not surprisingly, there is typically no unique homogenization procedure for a given characteristic. In this paper, we propose and adopt a particular homogenization methodology to determine a continuum-scale sea ice rheology from consideration of the interaction of ice types within a representative region. An example of an alternative approach is that of *Hopkins* [1996] who has

[1]Centre for Polar Observation and Modelling, Department of Earth Sciences, University College London, London, UK.
[2]British Antarctic Survey, Cambridge, UK.
[3]Mineral, Ice and Rock Physics Laboratory and Centre for Polar Observation and Modelling, Department of Earth Sciences, University College London, London, UK.

0148-0227/06/2005JC002996

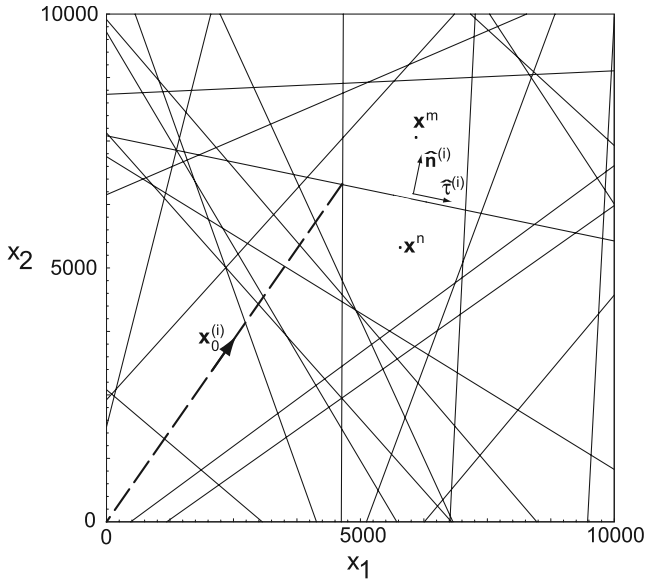

Figure 1. Definition diagram for two adjacent floes, with unit normal ($\hat{\mathbf{n}}^i$) and tangent vectors ($\hat{\boldsymbol{\tau}}^i$) for crack i, associated floe centroids with position vectors $\mathbf{x}^m$ and $\mathbf{x}^n$ ($m < n$), and the position vector of the point on the crack from which arc-length is measured $\mathbf{x}_0^i$. The length of the ith crack is l^i.

determined a plastic yield curve at the continuum-scale by means of a discrete element simulation of the interaction of floes using prescribed viscous-elastic-plastic force laws.

[5] In section 2, we describe in detail the homogenization methodology we use to determine the continuum-scale sea ice stress, and the particular material yield curves that we investigate. In section 3, we describe results for the case in which the sea ice floes are assumed to be squares as these results are both representative of a more realistic geometry and can be obtained largely analytically. In section 4, we consider the cases in which the sea ice floes are all diamond shaped or the individual floes have the shape of randomly-determined, irregular convex polygons. In section 5, we present an continuum-scale, lemon-shaped yield curve obtained by averaging over many realisations of floe configurations and using a viscous-plastic material rheology that is suitable for direct inclusion into a GCM. Finally, in section 6, we summarize and discuss our results in light of their implications for high-resolution sea ice modeling.

2. Method for Determination of Continuum-Scale Sea Ice Rheology

[6] In this section we introduce the method that is used to determine the continuum-scale sea ice rheology from the imposed subcontinuum scale material rheology and geometry of our representative region. This method was first discussed by *Feltham et al.* [2002] and is appropriate for compact ice covers as are typical in the central pack for most of the year; alternative approaches are appropriate for more disperse ice covers as are seen in the marginal ice zone [e.g., *Shen et al.*, 1987; *Feltham*, 2005]. In order to develop a continuum-scale rheology, we consider a region $\mathcal{R}$ of dimensions of 10 km $\times$ 10 km containing a collection of ice floes (typical area of, say, 1 km^2) separated by thin, rectilinear regions of thinner ice (leads). The continuum-scale rheology of this representative sea ice mixture is determined by imposing certain strain rates on the region $\mathcal{R}$, and calculating the stress required to cause this deformation. In order to do this, we use a kinematic model that relates the deformation of the constituents inside $\mathcal{R}$ to the deformation of the region as a whole [*Moritz and Ukita*, 2000]. Since the leads are weaker than the floes, these will preferentially fail so that the composite strain rate of $\mathcal{R}$ is (almost) entirely accomplished by deformation of the leads (the floes are very nearly rigid [e.g., *Gray and Morland*, 1994]). From the strain rate in a lead, we use a material rheology, or constitutive law, to determine the lead stress. The material rheology corresponds to the rheology of sea ice that would be measured in a laboratory or ice tank under suitable conditions. The geophysical, continuum-scale, mean stress field over the region $\mathcal{R}$ is then calculated from the area-weighted sum of the local lead stresses. By varying the imposed, continuum-scale velocity field $\mathbf{u}$, we determine the continuum-scale constitutive behavior of the composite sea ice.

[7] In this section, we first describe how we determine the geometry of our representative region. Then, we describe the kinematic model, which determines how the constituents of the continuum element move relative to one another. We then describe how we can use the kinematic model to determine the continuum-scale stress using a given material rheology. Finally, we describe the general form of the material rheologies considered, with the particular rheologies used described in Appendix A.

2.1. Geometry of Our Representative Region

[8] Consider a finite region of sea ice $\mathcal{R}$ assumed to contain relatively thick ice floes separated by cracks or leads containing relatively thin ice. The region $\mathcal{R}$ is partitioned into a tiling of the plane consisting of convex polygons formed by straight lines traversing the region $\mathcal{R}$, as in *Moritz and Ukita* [2000] (see Figure 1). There are J cracks indexed by $i = 1,\ldots,J$, and M floes indexed by $m = 1,\ldots,M$ and there is a one-to-one mapping between pairs of floes (m,n) and the ith crack, assuming (for definiteness) that $m < n$ [*Moritz and Ukita*, 2000]. Each crack is assumed to have a fixed width w^i and is assumed to contain ice with a thickness of h^i. Let the length of crack i be l^i and let $\mathbf{x}^m$ and $\mathbf{x}^n$ be the position vectors of the centroids of the convex polygonal floes m and n respectively, associated with crack i. We define $\hat{\mathbf{n}}^i$ to be the unit normal vector to crack i, such that $\hat{\mathbf{n}}^i$ points from floe n toward floe m and $\hat{\mathbf{k}}^i$ is the vertical unit vector pointing out of the tiling. On a given crack i, $\mathbf{x}(s) = \mathbf{x}_0^i + s\,\hat{\boldsymbol{\tau}}^i$ ($s \in [0, l^i]$) is the position of a point parameterized by its distance s from one end of the crack $\mathbf{x}_0^i$ in direction $\hat{\boldsymbol{\tau}}^i$, where $\hat{\boldsymbol{\tau}}^i$ is the unit tangent vector to crack i. If we define $\{\hat{\boldsymbol{\tau}}^i, \hat{\mathbf{n}}^i, \hat{\mathbf{k}}^i\}$ to be a right-handed orthonormal basis, then the direction of the tangent vector $\hat{\boldsymbol{\tau}}^i$ is specified and the location of $\mathbf{x}_0^i$ is fixed.

[9] In this paper we consider several different tilings of the plane: square tiles; diamond tiles; and a random tiling. For a simple geometry (e.g. squares) the positions of the lines is specified by the smallest positive angle β between the x_1-axis and a particular crack, and we assume that a vertex of a square tile is located at the origin (see Figure 2).

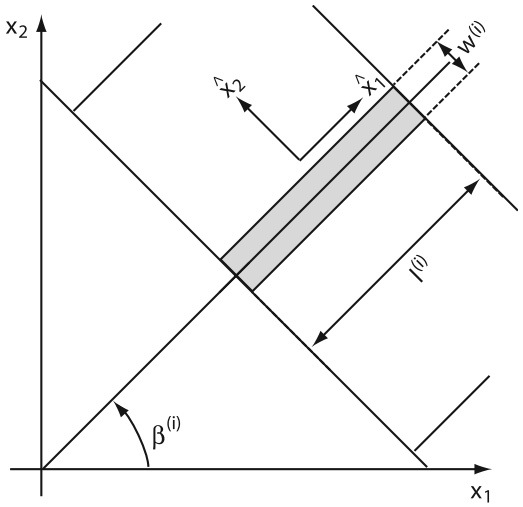

Figure 2. Definition diagram for lead i, of length l^i and width w^i, oriented at β^i relative to the principle axes of the large-scale strain-rate.

The orientation and position of the squares will influence the number and shape of partial square floes in our square domain, although this only has limited effect on the derived results when there are a sufficient number of completely square tiles within the domain. For a random geometry, we use the Poisson line process to specify the set of lines, so that the number of lines inside the region $\mathcal{R}$ is determined by the mean of a Poisson distribution (which we take to be 10 for our 10 km^2 standard domain); the location of a particular point on the line is determined from a uniform distribution on $\mathcal{R}$, and the direction of each line is specified by a uniform distribution on $[0, \pi]$. Once the lines in the plane are specified, the tiling of the region $\mathcal{R}$ is specified by those lines that are interior to $\mathcal{R}$ (in our case we use a square region). The area of the floes in the region $\mathcal{R}$ is $A(\mathcal{R})$ and does not account for the area of the cracks, which we specify separately.

2.2. Kinematic Model

[10] The kinematic model that we use is the same as that used by *Moritz and Ukita* [2000] and relates the motion of the constituents within our representative region to the strain rate imposed on the region as a whole. *Moritz and Ukita* [2000] used the kinematic model to estimate the *ridging*, *sliding*, and *opening* coefficients that occur in the rate of work equation that describes the rate of transfer of kinetic energy to internal energy per unit area of the ice cover. Estimating these coefficients enabled *Moritz and Ukita* [2000] to calculate the yield curve using a technique of minimization of maximum shear stress, and the same principle has been employed when explicitly incorporating the role of sliding friction between floes into basin-scale simulations [*Wilchinsky and Feltham*, 2004a; *Wilchinsky et al.*, 2006]. We do not take this approach here and instead use the kinematic model to determine the strain rate in the leads separating floes and calculate the lead stresses from these strain rates and a material rheology. For completeness, we describe the kinematic model here.

[11] It is assumed that the continuum-scale motion of the sea ice is defined by a continuously differentiable velocity field u_j (j = 1, 2) [*Moritz and Ukita*, 2000]. The relative motion of the sea ice in a small neighborhood of an arbitrary origin is given by a Taylor series expansion of the velocity field, neglecting second order and higher terms, so that

$$u_j(x_k) = u_{j,k}x_k + u_j(0), \tag{1}$$

where x_k is the position vector, $u_{j,k}$ is the velocity deformation tensor and the summation convention is used.

[12] The strain-rate is given by

$$\dot{\epsilon}_{jk} = \frac{u_{j,k} + u_{k,j}}{2}, \tag{2}$$

and the first and second invariants of the strain-rate are given by $\dot{\epsilon}_I = \dot{\epsilon}_{ii}$, and $\dot{\epsilon}_{II} = ((\dot{\epsilon}_{11} - \dot{\epsilon}_{22})^2 + 4\dot{\epsilon}_{12}^2)^{1/2}$. The alternative pair of strain-rate invariants $|\dot{\epsilon}|$ and θ are related to the first and second invariants of the strain-rate by $\dot{\epsilon}_I = |\dot{\epsilon}| \cos\theta$ and $\dot{\epsilon}_{II} = |\dot{\epsilon}| \sin\theta$. The parameter θ parameterizes the ratio of shear to divergence of the imposed global strain rate, with $\theta = 0$ corresponding to pure divergence and $\theta = \pi$ corresponding to pure convergence.

[13] If the coordinate system is assumed to be aligned with the principal axes of the strain-rate, the velocity deformation tensor can be written as a linear sum of the strain-rate and vorticity [*Moritz and Ukita*, 2000], of which only the strain-rate affects instantaneous deformation. Without loss of generality we may set the vorticity equal to zero, so that the components of the continuum-scale velocity field that influence continuum-scale stress and the instantaneous rate of ice deformation at any point $\mathbf{x}$ may be written as

$$\begin{aligned}\mathbf{u}(\mathbf{x}) - \mathbf{u}(\mathbf{0}) &= (\nabla\mathbf{u})\mathbf{x} \\ &= \frac{|\dot{\epsilon}|}{2}\begin{pmatrix}\cos\theta + \sin\theta & 0 \\ 0 & \cos\theta - \sin\theta\end{pmatrix}\begin{pmatrix}x_1 \\ x_2\end{pmatrix},\end{aligned} \tag{3}$$

where $\mathbf{x} = (x_1, x_2)^T$ are coordinates with respect to the principal axes of the strain-rate, and $|\dot{\epsilon}|$ and θ are strain-rate invariants [*Moritz and Ukita*, 2000].

[14] Since we are considering a densely packed ice cover, we suppose that the floes do not spin relative to the representative region comprising the collection of floes. It is possible that the representative region as a whole is undergoing rigid body rotation but this does not affect the estimate of continuum-scale stress.

[15] The translational velocity of a floe is equal to the continuum-scale velocity evaluated at the position of its centroid $\mathbf{x}^m$ so that the velocity of the mth floe is given by

$$\mathbf{v}^m = (\nabla\mathbf{u})\mathbf{x}^m. \tag{4}$$

The velocity jump across an individual crack $\Delta\mathbf{v}^i$ is required to determine the instantaneous rates of ice deformation in the crack. At each point along the ith crack, the velocity jump across the crack is

$$\Delta\mathbf{v}^i = \mathbf{v}^m - \mathbf{v}^n, \tag{5}$$

where m and n refer to the floes either side of the crack. Using the same notation as *Moritz and Ukita* [2000], we

define the normal component of relative velocity of the ith crack as

$$\xi^i = \Delta\mathbf{v}^i \cdot \hat{\mathbf{n}}^i, \tag{6}$$

and the tangential component of relative velocity of the ith crack as

$$\chi^i = \Delta\mathbf{v}^i \cdot \hat{\boldsymbol{\tau}}^i. \tag{7}$$

[16] The sea ice in each crack is assumed to deform plastically, with no deformation of the floes, which are treated as rigid. In the cracks at the rigid floe boundaries, the plastically deforming ice is assumed to move at the same velocity as the boundaries of the rigid floes. Therefore we can use the relative normal and tangential velocities to estimate the strain-rate in each crack. We use a crack coordinate system which has axes aligned with the crack $(\hat{x}_1, \hat{x}_2)$, such that $\hat{x}_1$ is parallel to the unit tangent vector $\hat{\tau}^i$ and $\hat{x}_2$ is parallel to the unit normal vector $\hat{\mathbf{n}}^i$. The components of the strain-rate tensor in the ith crack $\hat{\dot{\epsilon}}^i_{jk}$ are estimated using the definition of the strain-rate (2) and are given by

$$\hat{\dot{\epsilon}}^i_{11} = 0. \tag{8}$$

$$\hat{\dot{\epsilon}}^i_{12} = \chi^i/(2w^i), \tag{9}$$

and

$$\hat{\dot{\epsilon}}^i_{22} = \xi^i/w^i, \tag{10}$$

where we have used the fact that the cracks are much longer than they are wide, i.e. $l^i \gg w^i$. The resulting first and second invariants of strain-rate in the ith crack are

$$\dot{\epsilon}^i_I = \frac{\xi^i}{w^i}, \text{ and} \tag{11}$$

$$\dot{\epsilon}^i_{II} = \frac{\sqrt{(\xi^i)^2 + (\chi^i)^2}}{w^i}, \tag{12}$$

and the alternative strain-rate invariant θ^i is given by

$$\theta^i = \tan^{-1}\left(\text{sign}(\xi^i)\sqrt{1 + \left(\frac{\chi^i}{\xi^i}\right)^2}\right), \tag{13}$$

which implies that $|\theta^i| \geq \pi/4$ because the square root term is always at least unity. This has immediate implications for any continuum-scale estimate of stress, since it implies that pure divergence is not possible within cracks, and the minimum value of $|\theta^i|$ corresponds to uniaxial extension across a crack.

2.3. Calculation of Continuum-Scale Sea Ice Stress

[17] The kinematic model relates the continuum-scale imposed strain-rate to the strain rate in each crack. We use an imposed material rheology of the ice in the cracks to determine the stress inside the cracks. These subcontinuum stresses are related to the continuum-scale using an area-weighted average in a manner similar to *Hibler and Schulson* [2000].

[18] The stress tensor in the ith crack in the crack coordinate system is denoted by $\hat{\sigma}^i_{jk}$, and in the continuum-scale coordinate system by σ^i_{jk}. The stresses in each coordinate system are related by

$$\sigma^i_{jk} = R_{\beta^i}\hat{\sigma}^i_{jk}R_{-\beta^i}, \tag{14}$$

where β^i is the angle between the axes of the continuum-scale coordinate system and the crack coordinate system measured positive anti-clockwise, and R_{β^i} is the two-dimensional rotation matrix with rotation angle β^i.

[19] The aim of our method is to estimate the continuum-scale stress from the imposed continuum-scale strain rate. It is the sum of stresses induced inside the plastically deforming cracks that contributes to the continuum-scale stress. This can be deduced using Signorini's mean stress theorem [e.g., *Gray and Morland*, 1994], since the tractions either side of a crack cancel each other out when applying the mean stress theorem to a region consisting of several floes. To estimate the continuum-scale stress from the stresses inside the cracks we use the formula

$$\sigma^*_{jk} = \frac{\sum_{i=1}^{N} w^i l^i \sigma^i_{jk}}{A(\mathcal{R}) + \sum_{i=1}^{N} l^i w^i}, \tag{15}$$

which is simply the area-weighted average of the stress inside the cracks as a proportion of the total area of the region (sum of floe areas plus sum of crack areas).

2.4. Material Rheology

[20] We consider the sea ice stresses within the cracks to be described using an isotropic plastic rheology and we use three particular yield curves in our analysis: the elliptic yield curve; a modified Coulombic elliptic yield curve [*Hibler and Schulson*, 2000]; and a linear, Coulombic yield curve. These yield curves are illustrated in Figure 3 and discussed in Appendix A.

[21] The constitutive law for stress in the plastically deforming ice inside the cracks is an isotropic tensor function of the form

$$\sigma^i_{jk} = 2\eta^i\dot{\epsilon}^i_{jk} + (\zeta^i - \eta^i)\dot{\epsilon}^i_I\delta_{jk} - \frac{P^i}{2}\delta_{jk}, \tag{16}$$

where ζ^i and η^i are the bulk and shear viscosities, respectively, which can depend upon the first and second strain-rate invariants $\dot{\epsilon}_I$ and $\dot{\epsilon}_{II}$, and P^i is the pressure. Equation (16) can be used to relate the first and second invariants of stress to the first and second invariants of the strain-rate so that

$$\sigma^i_I = \zeta^i\dot{\epsilon}^i_I - \frac{P^i}{2}, \text{and} \tag{17}$$

$$\sigma^i_{II} = \eta^i\dot{\epsilon}^i_{II}, \tag{18}$$

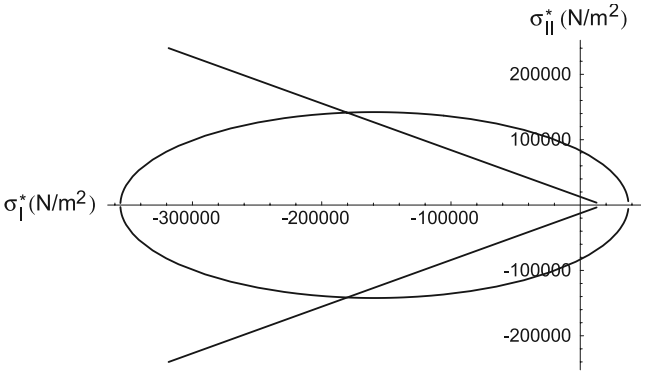

Figure 3. Yield curves at subcontinuum scale. Shown are the elliptic, linear, and modified-elliptic yield curves. The modified-elliptic yield curve consists of the linear yield curve to the right of the points of intersection with the ellipse, and the elliptical yield curve to the left of the intersection points.

where the stress invariants are defined analogously to the strain rate invariants, $\sigma_I^i = \frac{1}{2}\,\sigma_{kk}^i$ and $\sigma_{II}^i = ((\sigma_{11}^i - \sigma_{22}^i)^2 + 4(\sigma_{12}^i)^2)^{1/2}$.

3. Results for Regular Array of Square Floes

[22] Using the methodology described in the preceding section, we relate the continuum-scale sea ice stress to the assumed subcontinuum scale, material rheology. We consider a representative region containing sea ice floes and cracks determined by a checker board-like tiling of equal sized squares separated by cracks of uniform thickness and width. By restricting ourself to this particular geometry, it is possible to derive analytical results. An average over an ensemble of stress calculations with square floes oriented uniformly with respect to the principal axes of strain rate yields results similar to the average over an ensemble of isotropic, random configurations of floes.

3.1. Results Independent of Material Yield Curve

[23] The cracks dividing the ice cover into square floes consist of two sets of parallel cracks, denoted i and $i\perp$, with an orientation relative to the principal axes of the continuum-scale strain-rate of β^i and $\beta^{i\perp} = \beta^i + \pi/2$, respectively (i.e. one set of cracks is perpendicular to the other). Using (3) and (4), we calculate the relative velocity of the floe centroids either side of a crack to be

$$\Delta\mathbf{v}^{i,i\perp} = \mathbf{v}^{m_{i,i\perp}} - \mathbf{v}^{n_{i,i\perp}} \tag{19}$$

$$= \frac{|\dot\epsilon| l}{2}\begin{pmatrix} -(\cos\theta + \sin\theta)\sin\beta^{i,i\perp} \\ (\cos\theta - \sin\theta)\cos\beta^{i,i\perp} \end{pmatrix}, \tag{20}$$

where $l^i = l^{i\perp} = l$, so that the relative normal velocity and relative tangential velocity are given by

$$\xi^{i,i\perp} = \frac{\dot\epsilon}{2} l\left(\cos\theta - \sin\theta\cos 2\beta^{i,i\perp}\right), \text{ and} \tag{21}$$

$$\chi^{i,i\perp} = -\frac{\dot\epsilon}{2} l \sin\theta \sin 2\beta^{i,i\perp}, \tag{22}$$

respectively. Equations (21) and (22) are independent of position, which means that the relative velocities in all parallel cracks are identical, so it suffices to examine only two arbitrary cracks that are perpendicular to each other.

[24] The strain rates in two perpendicular cracks are estimated using equations (8)–(10), (21) and (22), and then converted to the continuum-scale coordinate system using rotation matrices in the same manner as for the continuum-scale stress (equation (14)). The resulting strain-rate tensors expressed in the continuum-scale coordinate system are given by

$$\dot\epsilon_{11}^i, \dot\epsilon_{22}^{i\perp} = \frac{|\dot\epsilon| l \sin^2\beta^i}{2w}(\cos\theta \pm \sin\theta), \tag{23}$$

$$\dot\epsilon_{12}^{i,i\perp} = \pm\frac{|\dot\epsilon| l \sin 2\beta^i}{4w}\cos\theta, \text{ and} \tag{24}$$

$$\dot\epsilon_{22}^i, \dot\epsilon_{11}^{i\perp} = \frac{|\dot\epsilon| l \cos^2\beta^i}{2w}(\cos\theta \mp \sin\theta), \tag{25}$$

where $w^i = w$ is the crack width. The first and second strain-rate invariants are given by

$$\dot\epsilon_I^{i,i\perp} = \frac{|\dot\epsilon| l}{2w}\left(\cos\theta \mp \sin\theta\cos 2\beta^i\right), \text{ and} \tag{26}$$

$$\dot\epsilon_{II}^{i,i\perp} = \frac{|\dot\epsilon| l}{2w}\sqrt{1 \mp \sin 2\theta\cos 2\beta^i}. \tag{27}$$

[25] The continuum-scale stress calculated for the square tiling on the domain $\mathcal{R}$ is given by (15) to be

$$\sigma_{jk}^* = \frac{\mathcal{W}^*}{2}\left(\sigma_{jk}^i + \sigma_{jk}^{i\perp}\right), \tag{28}$$

where

$$\mathcal{W}^* = \frac{2\sum_{i=1}^{N^*} l^i w^i}{A(\mathcal{R}) + 2\sum_{i=1}^{N^*} l^i w^i}, \tag{29}$$

and N^* is the number of pairs of orthogonal cracks inside the domain $\mathcal{R}$. Note that since $w^i = w$, $l^i = l$, it follows that $\sum_{i=1}^{N^*} l^i w^i = N^* lw$. We are neglecting the contribution to the continuum-scale stress estimate from cracks that do not form orthogonal pairs, e.g. in the case when $\beta^i \neq j\pi/2$ ($j = 0, 1, 2, \ldots$) there are nonsquare tiles in the domain. This is a reasonable assumption since for sufficiently large domains the overall stress will be dominated by the stresses from the square floes.

3.1.1. Alignment of Continuum Stress and Strain Rate Principal Axes

[26] Generally, the axes of continuum-scale sea ice stress are not aligned with the axes of continuum-scale strain rate.

In this case, as θ is varied the continuum-scale sea ice stress moves along a trajectory $\{\sigma^*_{11}, \sigma^*_{12}, \sigma^*_{22}\}$ and it is not possible to represent the plastic behavior with a two-dimensional yield curve. In this case, we have an anisotropic continuum-scale sea ice rheology.

[27] However, it is possible to consider particular orientations of the square floes with respect to the principal axes of strain rate for which the principal axes of continuum-scale stress and strain rate align, i.e. $\sigma^*_{12} = 0$.

[28] From equation (28), we see this can occur in one of two ways: Either each individual component of the shear stress is zero (i.e. $\sigma^i_{12} = \sigma^{i\perp}_{12} = 0$), or if the components of shear stress cancel each other out (i.e. $\sigma^i_{12} + \sigma^{i\perp}_{12} = 0$).

[29] Since the material rheologies we consider are of Reduced Reiner-Rivlin form (equation (16)) so that $\sigma_{12} = 2\eta\dot{\epsilon}_{12}$, we see from equation (24) that the individual components of shear stress in each orthogonal crack become zero when $\beta^i = j\pi/4$, for $j = 0, 1, 2, \ldots$. Therefore we have two particular orientations that result in no shear stress at the large-scale: the first is where the cracks are aligned with principal axes of the strain-rate tensor; and the second is where the cracks are aligned at $\pi/4$ to the principal axes of the strain-rate tensor.

[30] We now consider the two cases in turn to determine the relationship between the subcontinuum scale material rheology and the continuum-scale material rheology.

[31] First, we consider the case when $\beta^i = \pi/4 + j\pi/2$, for $j = 0, 1, 2, \ldots$. In this case the strain-rates invariants in perpendicular cracks are identical and from (26) and (27) are given by

$$\dot{\epsilon}^i_I = \dot{\epsilon}^{i\perp}_I = \frac{|\dot{\epsilon}|l\cos\theta}{2w} \text{ and} \tag{30}$$

$$\dot{\epsilon}^i_{II} = \dot{\epsilon}^{i\perp}_{II} = \frac{|\dot{\epsilon}|l}{2w}, \tag{31}$$

so that $\eta^i = \eta^{i\perp}$ and $\zeta^i = \zeta^{i\perp}$. Therefore, using equations (23)–(27) it follows from (28), the global stress is given by

$$\sigma^*_{jk} = \mathcal{W}^*\sigma^i_{jk}\delta_{jk}. \tag{32}$$

[32] Using (17), (18), and (30)–(32), we can relate the invariants of the continuum-scale sea ice stress to the invariants of the lead stresses as

$$\sigma^*_I = \mathcal{W}^*\sigma^i_I, \text{ and} \tag{33}$$

$$\sigma^*_{II} = -\mathcal{W}^*\sigma^i_{II}\sin\theta. \tag{34}$$

[33] For any material yield curve determining $\{\sigma^i_I, \sigma^i_{II}\}$, the continuum-scale maximum shear stress is zero in pure convergence ($\theta = \pi$) and pure divergence ($\theta = 0$). Material yield curves that are convex with the greatest value of σ^i_{II} in pure shear ($\theta = \pi/2$) lead to convex continuum-scale yield curves.

[34] Second, we consider the case when $\beta^i = j\pi/2$, for $j = 0, 1, 2, \ldots$. In this case the strain-rate invariants in the cracks are determined from equations (26) and (27) to be

$$\dot{\epsilon}^{i,i\perp}_I = \frac{|\dot{\epsilon}|l}{2w}\left(\cos\theta - (-1)^j\sin\theta\right), \tag{35}$$

$$\dot{\epsilon}^{i,i\perp}_{II} = \frac{|\dot{\epsilon}|l}{2w}\left|\cos\theta - (-1)^j\sin\theta\right|. \tag{36}$$

Without loss of generality we can assume that the ith crack corresponds to even values of j, so that the nonzero components of global stress are given by

$$\sigma^*_{11} = \mathcal{W}^*\frac{|\dot{\epsilon}|l}{4w}\left\{(\cos\theta - \sin\theta)\left(\zeta^i - \eta^i\right) + (\cos\theta + \sin\theta)\left(\zeta^{i\perp} + \eta^{i\perp}\right)\right\} - \mathcal{W}^*\frac{P^i}{2}, \tag{37}$$

$$\sigma^*_{22} = \mathcal{W}^*\frac{|\dot{\epsilon}|l}{4w}\left\{(\cos\theta - \sin\theta)\left(\zeta^i + \eta^i\right) + (\cos\theta + \sin\theta)\left(\zeta^{i\perp} - \eta^{i\perp}\right)\right\} - \mathcal{W}^*\frac{P^i}{2}, \tag{38}$$

so that the global stress invariants are given by

$$\sigma^*_I = \mathcal{W}^*\frac{|\dot{\epsilon}|l}{4w}\left\{(\cos\theta - \sin\theta)\zeta^i + (\cos\theta + \sin\theta)\zeta^{i\perp}\right\} - \mathcal{W}^*\frac{P}{2}, \tag{39}$$

$$\sigma^*_{II} = \mathcal{W}^*\frac{|\dot{\epsilon}|l}{4w}\left\{-(\cos\theta - \sin\theta)\eta^i + (\cos\theta + \sin\theta)\eta^{i\perp}\right\}. \tag{40}$$

3.1.2. Ensemble of Orientations

[35] We now consider a uniform ensemble of orientations of the square tiles ranging from $\beta^i = 0$ to $\beta^i = \pi/2$ and define the average continuum-scale stress to be

$$\langle\sigma^*_{jk}\rangle = \frac{2}{\pi}\int_0^{\pi/2}\frac{\mathcal{W}^*}{2}\left(\sigma^i_{jk} + \sigma^{i\perp}_{jk}\right)\mathrm{d}\beta^i, \tag{41}$$

which is simply the expected value of the continuum-scale stress under the assumption that the orientation angle β^i is a uniform random variable on [0, π/2].

[36] The stress σ^i_{jk} depends on the orientation angle β^i through its relationship with the strain-rate $\dot{\epsilon}^i_{jk}$. The strain-rates in the ith crack are related to the strain-rates in the $i\perp$th crack by $\dot{\epsilon}^i_{jk}(\beta^i) = \dot{\epsilon}^{i\perp}_{jk}(\pi/2 + \beta^i)$, which implies that $\eta^i(\beta^i) = \eta^{i\perp}(\pi/2 + \beta^i)$, $\zeta^i(\beta^i) = \zeta^{i\perp}(\pi/2 + \beta^i)$ and hence $\sigma^i_{jk}(\beta^i) = \sigma^{i\perp}_{jk}(\pi/2 + \beta^i)$. Thus

$$\begin{aligned}\langle\sigma^*_{jk}\rangle &= \frac{2}{\pi}\int_0^{\pi/2}\frac{\mathcal{W}^*}{2}\left(\sigma^i_{jk}(\beta^i) + \sigma^{i\perp}_{jk}(\beta^i)\right)\mathrm{d}\beta^i \\ &= \frac{\mathcal{W}^*}{\pi}\left(\int_0^{\pi/2}\sigma^i_{jk}(\beta^i)\mathrm{d}\beta^i + \int_0^{\pi/2}\sigma^i_{jk}(\beta^i - \pi/2)\mathrm{d}\beta^i\right) \\ &= \frac{\mathcal{W}^*}{\pi}\left(\int_0^{\pi/2}\sigma^i_{jk}(\beta^i)\mathrm{d}\beta^i + \int_0^{\pi/2}\sigma^i_{jk}(-\beta^*)\mathrm{d}\beta^*\right)\end{aligned}$$

where $\beta^* = \pi/2 - \beta^i$

$$= \frac{\mathcal{W}^*}{\pi}\left(\int_0^{\pi/2}\left(\sigma^i_{jk}(\beta^*) + \sigma^i_{jk}(-\beta^*)\right)\mathrm{d}\beta^*\right). \tag{42}$$

[37] The definitions of the stress in the ith crack (16) together with the definitions of the strain-rates and their invariants for the square floes (23)–(27) can be seen to yield the relationships: $\sigma^i_{11}(\beta^*) = \sigma^i_{11}(-\beta^*)$; $\sigma^i_{22}(\beta^*) = \sigma^i_{22}(-\beta^*)$; and $\sigma^i_{12}(\beta^*) = -\sigma^i_{12}(-\beta^*)$. It follows that $\langle\sigma_{12}{}^*\rangle = 0$ and so the invariants of stress for the ensemble average are given by

$$\langle\sigma^*_I\rangle = \frac{2\mathcal{W}^*}{\pi}\int_0^{\pi/2}\sigma^i_I \mathrm{d}\beta^i, \tag{43}$$

and

$$\langle\sigma^*_{II}\rangle = \frac{2\mathcal{W}^*}{\pi}|\int_0^{\pi/2}\left(\sigma^i_{11}-\sigma^i_{22}\right)\mathrm{d}\beta^i|. \tag{44}$$

3.2. Results for Particular Yields Curves

3.2.1. Elliptic Yield Curve

[38] In the case of the elliptical yield curve with squares oriented at $\pi/4 + j\pi/2$ to the principal axes of the continuum-scale strain-rate it can be shown using (A2), (A3), (26) and (27) that the bulk viscosity is given by

$$\zeta^i = \zeta^{i\perp} = \frac{P^*w}{|\dot\epsilon| l\sqrt{\cos^2\theta + 1/e^2}}, \tag{45}$$

where $P^* = P^{*i} = P^{*i\perp}$ and the shear viscosity is given by

$$\eta^i = \eta^{i\perp} = \frac{P^*w}{e^2|\dot\epsilon| l\sqrt{\cos^2\theta + 1/e^2}} \tag{46}$$

so that, using (17), (18), (30), (31), (33) and (34), the global invariants of the continuum-scale stress are given by

$$\sigma^*_I = \frac{\mathcal{W}^*P^*\cos\theta}{2\sqrt{\cos^2\theta + 1/e^2}} - \mathcal{W}^*\frac{P}{2}, \text{ and} \tag{47}$$

$$\sigma^*_{II} = -\frac{\mathcal{W}^*P^*\sin\theta}{2e^2\sqrt{\cos^2\theta + 1/e^2}}, \tag{48}$$

where $P = P^i = P^{i\perp}$.

[39] Eliminating the dependence on θ between (47) and (48) yields

$$\left(\frac{2\sigma^*_I + \mathcal{W}^*P}{\mathcal{W}^*P^{*i}}\right)^2(1+1/e^2) + \left(\frac{2e\sigma^*_{II}}{\mathcal{W}^*P^{*i}}\right)^2 = 1. \tag{49}$$

[40] Therefore, when the floes are oriented at $\pi/4$, the resulting yield curve at the continuum scale has the same form as the yield curve at the subcontinuum scale (equation (A1)) with the ratio of the major and minor axes of the ellipse becoming $\sqrt{(1+e^2)/e^4}$. This can be thought of as a kind of conditional scale invariance.

[41] In the case of the elliptical yield curve with squares oriented at $j\pi/2$ to the principal axes of the continuum-scale strain-rate the viscosities can be shown using (A2), (A3), (26) and (27) to be

$$\zeta^{i,i\perp} = \frac{P^*w}{|\dot\epsilon| l\sqrt{1+1/e^2}\sqrt{1-(-1)^j\sin 2\theta}}, \tag{50}$$

and

$$\eta^{i,i\perp} = \frac{P^*w}{|\dot\epsilon| le^2\sqrt{1+1/e^2}\sqrt{1-(-1)^j\sin 2\theta}}. \tag{51}$$

[42] Therefore, from (39) and (40), the global invariants of the stress are given by

$$\sigma^*_I = \frac{\mathcal{W}^*P^*}{4\sqrt{1+1/e^2}}\{h(\theta)+g(\theta)\} - \mathcal{W}^*\frac{P}{2}, \tag{52}$$

$$\sigma^*_{II} = \frac{\mathcal{W}^*P^*}{4e^2\sqrt{1+1/e^2}}\{-h(\theta)+g(\theta)\}, \tag{53}$$

where $h(\theta)$ and $g(\theta)$ can be written explicitly as

$$h(\theta) = \frac{\cos\theta - \sin\theta}{\sqrt{1-\sin 2\theta}} = \begin{cases} 1 & \theta \in \left(-\frac{3\pi}{4} - (j+1)\pi, \frac{\pi}{4} - j\pi\right) \\ -1 & \theta \in \left(\frac{\pi}{4} - j\pi, \frac{\pi}{4} - (j-1)\pi\right) \end{cases} \tag{54}$$

and

$$g(\theta) = \frac{\cos\theta + \sin\theta}{\sqrt{1+\sin 2\theta}} = \begin{cases} 1 & \theta \in \left(-\frac{\pi}{4} - (j+1)\pi, -\frac{\pi}{4} - j\pi\right) \\ -1 & \theta \in \left(-\frac{\pi}{4} - j\pi, -\frac{\pi}{4} - (j-1)\pi\right) \end{cases} \tag{55}$$

where $j = 0, 1, 2, \ldots$.

[43] Using the definition of h and g, we see that the global invariants of the stress yield four discrete points given by

$$(\sigma^*_I, \sigma^*_{II}) = \begin{cases} \left(\frac{\mathcal{W}^*P^*}{2\sqrt{1+1/e^2}} - \mathcal{W}^*\frac{P}{2}, 0\right) & \theta \in \left(-\frac{\pi}{4}, \frac{\pi}{4}\right) \\ \left(-\mathcal{W}^*\frac{P}{2}, \frac{\mathcal{W}^*P^*}{2e^2\sqrt{1+1/e^2}}\right) & \theta \in \left(\frac{\pi}{4}, \frac{3\pi}{4}\right) \\ \left(-\frac{\mathcal{W}^*P^*}{2\sqrt{1+1/e^2}} - \mathcal{W}^*\frac{P}{2}, 0\right) & \theta \in \left(\frac{3\pi}{4}, \pi\right) \text{ and } \theta \in \left(-\frac{3\pi}{4}, -\pi\right) \\ \left(-\mathcal{W}^*\frac{P}{2}, -\frac{\mathcal{W}^*P^*}{2e^2\sqrt{1+1/e^2}}\right) & \theta \in \left(-\frac{\pi}{4}, -\frac{3\pi}{4}\right). \end{cases} \tag{56}$$

[44] Figure 4 shows the yield curves for the two particular orientations of the square sea ice floes. For the square domain $\mathcal{R}$ of side 10 km with crack widths $w = 10$ m, and crack lengths $l = 1000$ m, the weighting factor $\mathcal{W}^*$ is set to a constant 0.0157. When the square floes are aligned with the continuum-scale strain-rate principal axes the yield curve consists of only four individual points, but we have shown it here to be interconnected by lines for ease of presentation.

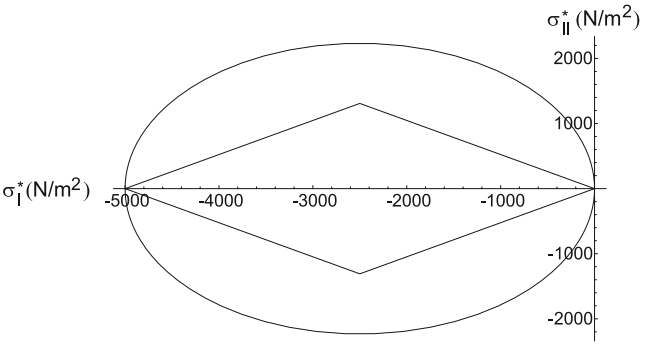

Figure 4. Yield curves in stress invariant space for two orientations of the square floes relative to the principal axes of the continuum-scale strain-rate (β^i = 0, π/4), obtained using the elliptic material rheology. The yield curve at $\beta^i = 0$ consists of four discrete points that are shown as joined lines.

[45] Considering the ensemble average of orientations using the subcontinuum scale elliptic material rheology, and substituting for $\sigma^i{}_{jk}$, using (17), (18), (A2), (A3), and (23)–(27), in equations (43) and (44) yields

$$\langle \sigma_I^* \rangle = \frac{\mathcal{W}^* P^*}{\pi} \int_0^{\pi/2} \frac{\cos\theta - \sin\theta \cos 2\beta^i}{\sqrt{(1+1/e^2)\left(1-\sin 2\theta \cos 2\beta^i\right) + \sin^2\theta\left(1-\cos^2 2\beta^i\right)}} \mathrm{d}\beta^i - \mathcal{W}^* \frac{P}{2}, \tag{57}$$

and

$$\langle \sigma_{II}^* \rangle = \frac{\mathcal{W}^* P^*}{2\pi e^2} \int_0^{\pi/2} \frac{\sin\theta + \cos\theta \cos 2\beta^i - \sin\theta \cos^2 2\beta^i}{\sqrt{(1+1/e^2)\left(1-\sin 2\theta \cos 2\beta^i\right) + \sin^2\theta\left(1-\cos^2 2\beta^i\right)}} \mathrm{d}\beta^i. \tag{58}$$

[46] Figure 5 shows the yield curve obtained using equations (57) and (58) with a weighting factor of 0.0157 as was used previously. The shape of the yield curve is described as a lemon shape, which remains similar in shape to the underlying elliptic material rheology. Also shown on the yield curve are the strain-rate vectors, which are seen to be almost normal to the yield curve.

3.2.2. Linear Yield Curve

[47] In the case of the linear yield curve with squares oriented at $\pi/4 + j\pi/2$ to the principal axes of the continuum-scale strain-rate the viscosities are given by (A2), (A3), (A8), (26) and (27) as

$$\zeta^i = \zeta^{i\perp} = \frac{P^* w}{|\dot{\epsilon}| l \sqrt{\cos^2\theta + 1/e^2}}, \tag{59}$$

which is the same as for the elliptic yield curve, and

$$\eta^i = \eta^{i\perp} = \frac{2Pw}{\alpha\beta|\dot{\epsilon}|l} - \frac{P^* w \cos\theta}{\beta|\dot{\epsilon}| l \sqrt{\cos^2\theta + 1/e^2}}. \tag{60}$$

[48] Therefore the global invariants of the stress are given by (33) and (34) to be

$$\sigma_I^* = \frac{\mathcal{W}^* P^* \cos\theta}{2\sqrt{\cos^2\theta + 1/e^2}} - \mathcal{W}^* \frac{P}{2} \text{ and} \tag{61}$$

$$\sigma_{II}^* = -\mathcal{W}^* \left(\frac{P \sin\theta}{\alpha\beta} - \frac{P^* \sin\theta\cos\theta}{2\beta\sqrt{\cos^2\theta + 1/e^2}} \right). \tag{62}$$

[49] Eliminating the dependence on θ in (61) and (62) yields

$$\sigma_{II}^* = \pm \sqrt{\frac{(\mathcal{W}^* P^*)^2 - (1+1/e^2)(2\sigma_I^* + \mathcal{W}^* P)^2}{(\mathcal{W}^* P^*)^2 - (2\sigma_I^* + \mathcal{W}^* P)^2}} \cdot \left(\frac{-\sigma_I^*}{\beta} + \frac{\mathcal{W}^* P}{\beta} \left\{ \frac{1}{\alpha} - \frac{1}{2} \right\} \right). \tag{63}$$

The resulting shape of the yield curve for the continuum scale is not the same as the yield curve for the subcontinuum scale except when e becomes very large. In the limit $e \to \infty$, we see that the linear yield curve is recovered with crack pressure P replaced by the continuum-scale pressure $\mathcal{W}^* P$ (see equation (A7)).

[50] In the case of the linear yield curve with squares oriented at $j\pi/2$ to the principal axes of the continuum-scale strain-rate the viscosities are given by (A2), (A3), (A8), (26) and (27) to be

$$\zeta^{i,i\perp} = \frac{P^* w}{|\dot{\epsilon}| l \sqrt{1+1/e^2} \sqrt{1-(-1)^j \sin 2\theta}}, \tag{64}$$

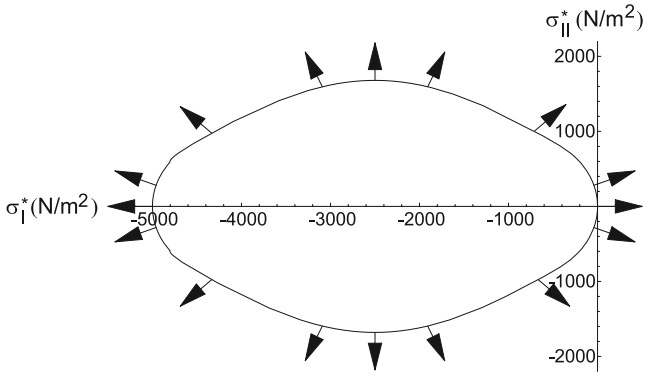

Figure 5. Yield curve and flow rule for uniform ensemble of realisations of the square geometry and elliptic material rheology.

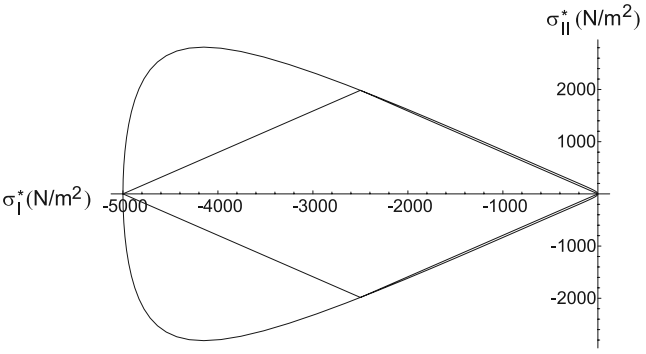

Figure 6. Yield curves in stress invariant space for two orientations of the square floes relative to the principal axes of the continuum-scale strain-rate (β^i = 0, π/4), obtained using the linear material rheology. The yield curve at β^i = 0 consists of four discrete points that are shown as joined lines.

and

$$\eta^{j,i\perp} = \frac{2Pw}{\alpha\beta|\dot{\epsilon}|l\sqrt{1-(-1)^j\sin 2\theta}} - \frac{P^*w\left(\cos\theta-(-1)^j\sin\theta\right)}{\beta|\dot{\epsilon}|l\sqrt{1+1/e^2}\left|1-(-1)^j\sin 2\theta\right|}. \quad (65)$$

[51] From (39), (40), (54), (55), (64) and (65) it can be shown that the global invariants of the stress yield four discrete points given by

$$(\sigma_I^*,\sigma_{II}^*) = \begin{cases} \left(\frac{P^*\mathcal{W}^*}{2\sqrt{1+1/e^2}} - \mathcal{W}^*\frac{P}{2}, 0\right) & \theta\in\left(-\frac{\pi}{4},\frac{\pi}{4}\right) \\ \left(-\mathcal{W}^*\frac{P}{2}, \frac{P\mathcal{W}^*}{\alpha\beta}\right) & \theta\in\left(\frac{\pi}{4},\frac{3\pi}{4}\right) \\ \left(-\frac{P^*\mathcal{W}^*}{2\sqrt{1+1/e^2}} - \mathcal{W}^*\frac{P}{2}, 0\right) & \theta\in\left(\frac{3\pi}{4},\pi\right) \text{ and } \theta\in\left(-\frac{3\pi}{4},-\pi\right) \\ \left(-\mathcal{W}^*\frac{P}{2}, -\frac{P\mathcal{W}^*}{\alpha\beta}\right) & \theta\in\left(-\frac{\pi}{4},-\frac{3\pi}{4}\right). \end{cases} \quad (66)$$

[52] Figure 6 shows the yield curves for the two particular orientations of the square sea ice floes. When the square floes are aligned with the continuum-scale strain-rate principal axes the yield curve consists of only four individual points, but we have shown it here to be interconnected by lines for ease of presentation.

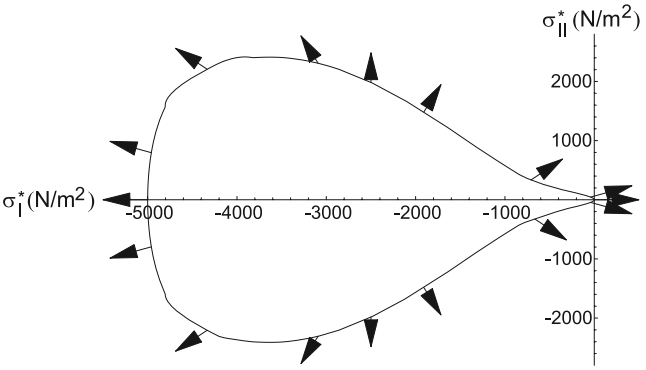

Figure 7. Yield curve and flow rule for uniform ensemble of realisations of the square geometry and linear material rheology.

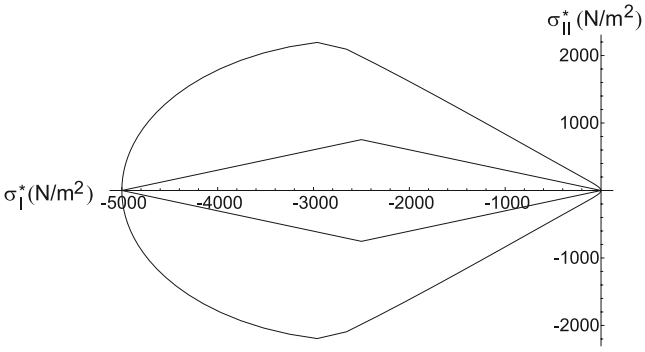

Figure 8. Yield curves in stress invariant space for two orientations of the square floes relative to the principal axes of the continuum-scale strain-rate (β^i = 0, π/4), obtained using the modified elliptic material rheology. The yield curve at β^i = 0 consists of four discrete points that are shown as joined lines.

[53] The ensemble-averaged yield curve for the linear material rheology was determined numerically (see Figure 7). The linear material rheology is interesting since at the subcontinuum scale for pure convergence the maximum shear stress is large, whereas at the continuum scale under pure convergence the maximum shear stress is zero. Also shown on the yield curve are the strain-rate vectors, which in this case are not normal as expected.

3.2.3. Modified Elliptic Yield Curve

[54] The resulting yield curve at the two particular orientations of β^i = 0 and π/4 are shown in Figure 8. Since the modified elliptic yield curve consists of the composition of the linear yield curve and the elliptic yield curve, the results for the modified elliptic yield curve are similar to the combination of the results for the elliptic and linear yield curves.

[55] The ensemble averaged yield curve for the modified elliptic material rheology was also determined numerically (see Figure 9). The strain-rate vectors are also shown, and again are not normal.

3.3. Anisotropic Results for Square Floes

[56] Here, we consider the situation of a regular array of square floes in which the ice in one set of parallel cracks is a

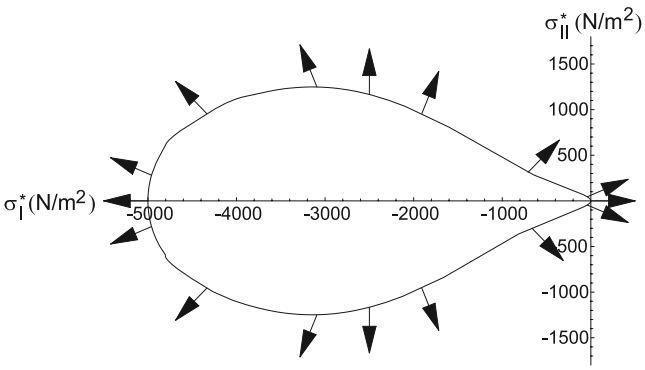

Figure 9. Yield curve and flow rule for uniform ensemble of realisations of the square geometry and modified elliptic material rheology.

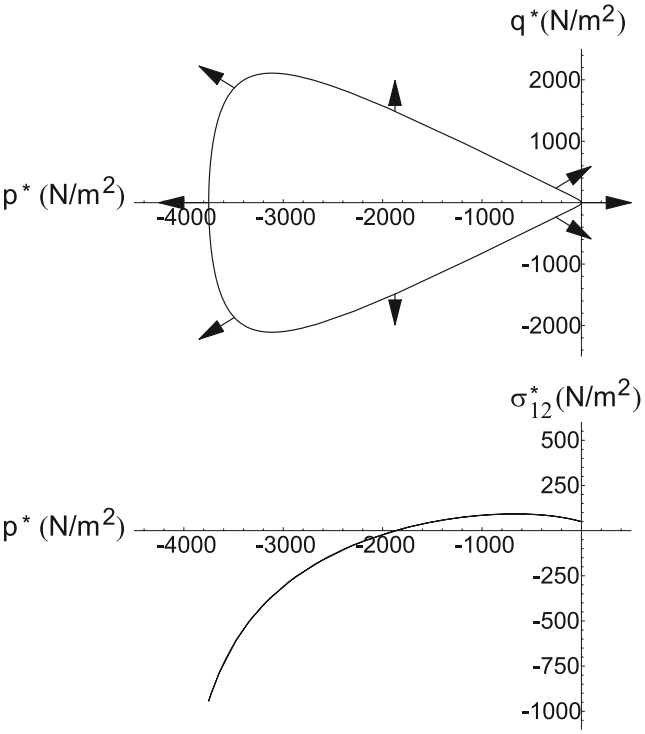

Figure 10. Yield curve projections onto $p^* - q^*$ and $p^* - \sigma_{12}^*$ planes for square geometry oriented at $\pi/4$ to the principal axes of the continuum-scale strain-rate and linear material rheology in the anisotropic case (anisotropy fact $\mu = 0.5$). The flow rule is also shown because the flow rule will be aligned with the $p^* - q^*$ plane.

factor of $\mu \neq 1$ times the thickness of the ice in the perpendicular set of parallel cracks. The factor of μ does not affect the strain rates in the cracks but does affect the stresses.

[57] We illustrate the role of anisotropy by considering the case in which the cracks are oriented at $\pi/4$ to the principal axes of strain rate for all θ. In this case, $\zeta^{i\perp} = \mu\zeta^i$ and $\eta^{i\perp} = \mu\eta^i$ for all the material yield curves, so that from equation (16) $\sigma_{jk}^{i\perp} = (-1 + 2\delta_{jk})\mu\sigma_{jk}^i$. Therefore, analogous to equation (32), the continuum-scale stress is given by

$$\sigma_{jk}^* = \mathcal{W}^* \left(\frac{1 + (2\delta_{jk} - 1)\mu}{2} \right) \sigma_{jk}^i, \tag{67}$$

where $\mathcal{W}^*$ is given by (29). (Equation (67) reduces to (32), upon setting $\mu = 1$.) Using (15)–(18) and (30), (31), we see that the average normal continuum-scale stress p^* and half the difference between the normal continuum-scale stresses q^* are given by

$$p^* = \mathcal{W}^* \frac{1+\mu}{2} \frac{\sigma_{11}^i + \sigma_{22}^i}{2} = \mathcal{W}^* \frac{1+\mu}{2} \sigma_I^i, \text{ and} \tag{68}$$

$$q^* = \mathcal{W}^* \frac{1+\mu}{2} \frac{\sigma_{11}^i - \sigma_{22}^i}{2} = -\mathcal{W}^* \frac{1+\mu}{2} \sigma_{II}^i \sin\theta, \tag{69}$$

and the shear stress is given by

$$\sigma_{12}^* = \frac{\mathcal{W}^*(1-\mu)}{4} \sigma_{II}^i \cos\theta. \tag{70}$$

The projections onto the $p^* - \sigma_{12}^*$ plane and the $q^* - \sigma_{12}^*$ plane satisfy

$$p^* = 2\frac{1+\mu\zeta^i}{1-\mu\eta^i}\sigma_{12}^* - \mathcal{W}^* \frac{1+\mu}{2}\frac{P^i}{2}, \text{ and} \tag{71}$$

$$\left(\frac{2q^*}{1+\mu}\right)^2 + \left(\frac{4\sigma_{12}^*}{1-\mu}\right)^2 = \left(\mathcal{W}^*\sigma_{II}^i\right)^2. \tag{72}$$

[58] In the case that ζ^i/η^i is independent of the continuum-scale alternative strain-rate invariant θ, which is true for the elliptic yield curve but not the linear yield curve or the linear portion of the modified elliptic yield curve, the projection onto the $p^* - \sigma_{12}^*$ plane is a straight line. Equation (72) tells us that the projection onto the $q^* - \sigma_{12}^*$ plane is given by points (parameterized by θ) that lie on ellipses centered on the origin with varying major and minor axes, whose ratio of major to minor axes remain constant.

[59] Figure 10 shows the results at the special orientation of $\beta^i = \pi/4$ with $\mu = 1/2$ for the linear material rheology. It can be clearly seen that the minimum value of the average normal stress is given by $(1 + \mu)/2$ times the isotropic case. As the anisotropy parameter tends to unity the shape of the plot of shear stress (σ_{12}^*) versus average normal stress (p^*) tends toward a straight line coincident with the p^* axis. As μ is increased above unity, the shape of the plot is reflected about the p^* axis, although the minimum average normal stress decreases.

4. Results for Diamond and Random Geometries

[60] We designed an algorithm using Mathematica that could accept arbitrary tilings of the plane, arbitrary yield curves and could impose continuum-scale strain-rates to numerically calculate the resulting continuum-scale stress. The results were found to have good agreement with the analytical calculations depending on the orientation of the square floes. Departures from analytical calculations were because the domain of interest was defined to be square with sides of length 10 km, so that there could be nonsquare floes inside the domain affecting the overall stress.

[61] Satellite observations of sea ice reveal that diamond-shaped floes are common [*Marko and Thomson*, 1977; *Erlingsson*, 1988]. Calculations using diamond-shaped floes (with smaller apex angle of 30 degrees and boundary lengths 1000 m) yielded results similar to those with square floes. However, the only orientations of the diamond geometry for which the continuum-scale shear stress becomes zero are when the diamond diagonals are parallel to the continuum-scale strain-rate principal axes. This is equivalent to the case of the square sea ice floes at $\pi/4$ to the principal axes of continuum-scale strain rate, and in both cases the reason that the continuum-scale shear stress is zero is because the shear stress between pairs of nonparallel

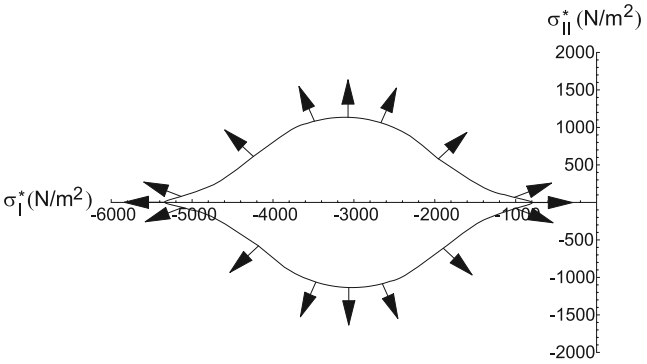

Figure 11. Yield curve and flow rule for ensemble of realisations of the diamond geometry using the elliptic material rheology.

cracks cancel. For more typical orientations of the diamonds, the continuum sea ice stress is not isotropic. A model treating the sea ice cover as a collection of diamonds that may be anisotropically distributed is described by *Wilchinksy and Feltham* [2006b]. An ensemble of realisations of the diamond geometry with uniform distribution of orientation leads to a yield curve for which the principal axes of continuum-scale stress and strain-rate are aligned (Figure 11).

[62] We also considered a random geometry generated using the Poisson line process [cf. *Thorndike*, 1987]. This produces an isotropically distributed pattern of cracks. The Poisson line process uses three independent distributions: The number of points inside the domain $\mathcal{R}$ is determined using the Poisson distribution; the location of each point is determined using a uniform distribution over $\mathcal{R}$; and the angle of the line that intersects each point relative to a fixed coordinate system is determined using a uniform distribution on $[0,\pi]$. For our 10 km $\times$ 10 km region $\mathcal{R}$ we used a mean of 10 points in the domain. An example of the random geometry is shown in Figure 1. For a large sample of cracks from repeated realisations on the domain the continuum-scale shear stress becomes approximately zero, and the yield curve obtained from a large ensemble of realisations is similar to the yield curve obtained using the ensemble of realisations of the square geometry (see Figure 12 for an example using the elliptic yield curve, see Figure 5). For a particular randomly-determined pattern of cracks, the calculated continuum-scale stress has a shear component in the coordinate system of the continuum strain rate that is of similar magnitude to the normal stresses, i.e. the stress law is not isotropic.

[63] The kinematic model affects the size and position of the yield curve in stress invariant space leading to a continuum-scale average normal stress that is marginally less than zero for continuum-scale pure divergence. This is because for a given crack the vector between the floe centroids (associated with the crack) are not necessarily orthogonal to the crack.

5. Continuum, GCM-Scale Rheology Derived From Ensemble Averaging

[64] An isotropic sea ice rheology has emerged from the results deduced using the ensemble average of both the square sea ice floes and the ensemble average of the random geometry. For computational convenience, a simple expression for this yield curve was determined using a least squares fit to the yield curve in Figure 5 given by

$$\sigma_{II}^2 = \mathcal{K}^2 \sin\left(-\frac{\pi\sigma_I}{P^{*cs}}\right), \tag{73}$$

where

$$\mathcal{K} = \frac{0.9815K(e^2/(1+e^2))\mathcal{W}^*P^{*i}}{\sqrt{1+e^{-2}}\pi e^2}. \tag{74}$$

where $K(m)$ is the Complete Elliptic Integral of the First Kind, and all other terms are as defined earlier. The flow rule for this yield curve can be approximated using the normal flow rule (see Figure 5). A comparison of this approximate yield curve with the exact yield curve is shown in Figure 13. The compressive strength of the sea ice at the continuum scale P^{*cs} (where *cs* stands for continuum scale) is related to the compressive strength at the subcontinuum scale P^{*i} by $P^{*cs} = \mathcal{W}^* P^{*i}$ (see equations (15) and (29)), and we estimate $\mathcal{W}^*$ to be 0.0157, which is true for square floes of length 1 km with crack width of 10 m. To achieve values of P^{*cs} at the continuum scale that are consistent with a recent estimate, $\sim$5000 N/m^2, determined from a

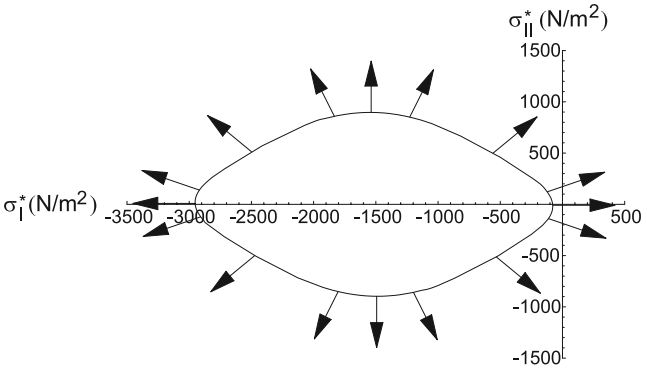

Figure 12. Yield curve and flow rule for ensemble of 100 realisations of the random geometry using the elliptic material rheology.

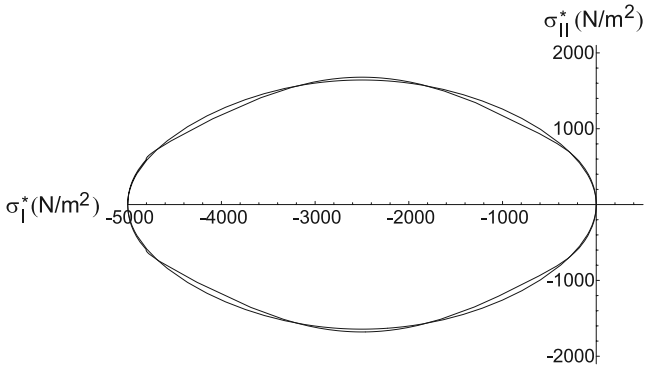

Figure 13. Comparison of yield curve obtained from ensemble average of square geometry (Figure 5) and yield curve obtained from the analytical approximation (equation (73)).

comparison of sea ice model simulations with a range of satellite data [*Miller et al.*, 2006], we have set $P^{*i} = 0.32 \times 10^6$ N/m^2, which is of the correct order of magnitude [*Cox and Richter-Menge*, 1984; *Weeks*, 1983]. This relationship between continuum-scale and subcontinuum scale ice strength is useful in extrapolating from laboratory-determined estimates of P^* [e.g., *Sammonds et al.*, 2005]. The continuum, lemon-shaped plastic yield curve may be considered to be an alternative to commonly-adopted yield curve shapes, such as the ellipse [*Hibler*, 1979], Coulombic ice-cream cone [*Tremblay and Mysak*, 1997] or modified Coulombic ellipse [*Hibler and Schulson*, 2000].

6. Summary and Discussion

[65] The method described in this paper allows us to calculate the continuum, GCM-scale sea ice rheology using the subcontinuum, material rheology of sea ice for a particular geometry of the arrangement of floes and leads.

[66] Our results showed that the principal axes of continuum-scale stress and strain-rate were generally not aligned except for specific arrangements of the floes and leads. By contrast, the principle axes of the averaged continuum-scale stress determined from averaging over an ensemble of either regular, or randomly-determined, geometrically isotropic geometries, were aligned with the principle axes of continuum-scale strain rate. These calculations revealed notable similarity between the yield curves for an ensemble of squares and irregular, convex polygons and these yield curves are similar to those obtained previously. For example, *Ukita and Moritz* [2000], who used a technique that minimizes maximum shear stress, found that when they neglected contributions from sliding of adjacent floes the yield curves for both an ensemble average of a random geometry and an ensemble average of a square geometry [*Moritz and Ukita*, 2000] were of a sine-lens shape, which is quite similar to the lemon-shaped yield curve (Figure 5) we determined for an ensemble average of the square geometry for the elliptic material rheology.

[67] Our calculations revealed a qualitative difference between the yield surfaces at different orientations of the square geometry with respect to the principle axes of continuum-scale strain rate; ranging from discrete points when the square floe boundaries aligned with the principal axes of the continuum-scale strain rate to a smooth yield curve, which was similar to the yield curve at the subcontinuum scale, when the square floe boundaries were aligned at $\pi/4$ to the principal axes of the continuum-scale strain-rate. This behavior contrasts with that observed for square floes by *Moritz and Ukita* [2000] who found yield curves that were qualitatively similar to one another as the orientation angle varied.

[68] An advantage of our homogenization methodology is that the steps by which the continuum-scale rheology is derived are explicit and transparent. The calculation of continuum-scale stress with ensemble-averaging of either a uniform distribution of square floes or an unbiased random tiling led to a rheology similar to that in current common usage, namely an isotropic plastic rheology with normal flow law. Although the lemon-shaped yield curve shape we obtained is suitable for direct inclusion into sea ice and climate models, we do not consider this to be the principal outcome of our analysis. Our homogenization procedure has enabled us to explore scaling relations between the subcontinuum and continuum scales and indicate the limitations of using a continuum isotropic, plastic rheology: (i) For square floes oriented at $\pi/4$ to the principal axes of strain rate, the calculated continuum-scale rheology was isotropic with a yield curve that had features in common with the material yield curve shape. For example, with the elliptical material yield curve, the continuum yield curve assumes an elliptical shape with altered aspect ratio. This can be thought of as a kind of conditional scale invariance. For more typical orientations of the floes in our continuum element, there is no obvious link between the material and continuum stress orientations. Probably a more useful scaling relation is that between the magnitude of stresses at the material scale (characterized by the ice strength parameter) and the magnitude of stresses at the continuum scale; (ii) Although we have presented particular geometries of the floe arrangement that lead to an isotropic continuum rheology, it is important to note that for typical floe arrangements the continuum-scale rheology is far from isotropic. Our averaging region was 10 km by 10 km, and our typical floe dimension was 1 km, so that typically our continuum region contained about 100 floes. It was only by averaging over approximately 100 different random realisations of the floe geometry that isotropy was obtained. This is equivalent to increasing the size of our averaging area to 100 km $\times$ 100 km and indicates that the application of an isotropic rheology below grid sizes of 100 km (for our floe size) is valid only in a statistical sense. The concept of an isotropic, continuum rheology valid only in an averaged sense over a sufficiently large continuum element was central to the development of the original AIDJEX model [*Coon et al.*, 1974] and has been noted by, among others, *Overland et al.* [1995]. It is only in recent years that advances in computer technology have enabled models to be run at sub-100 km resolutions. An anisotropic model designed for application to sub-100 km lengthscales has been developed by *Wilchinsky and Feltham* [2004b, 2006a, 2006b] and associated frictional sliding in leads formed in an ice tank measured by *Sammonds et al.* [2005]. Although the adoption of an isotropic rheology at sub-100 km resolutions may be suitable for climate prediction (in which the results are averaged over an ensemble), our calculations indicate this is not useful for detailed prediction of ice dynamics, e.g. the formation and evolution of linear kinematic features.

Appendix A: Material Yield Curves

A1. Elliptic Yield Curve

[69] The continuum-scale, viscous-plastic sea ice rheology with elliptic yield curve and normal flow rule introduced by *Hibler* [1979] has been widely used in sea ice simulations since its introduction. This rheology is appropriate to sea ice treated as a continuum on a large scale, e.g. 100 km, but it has also been suggested that this rheology is appropriate as a description of the material behavior of sea ice on much smaller, laboratory, scales [e.g., *Hibler and Schulson*, 2000], although with a slightly modified ice strength and

yield curve aspect ratio. For this reason, we consider a material rheology given by the elliptic yield curve and flow rule described in *Hibler and Schulson* [2000], which allows the possibility of tensile stress. For the ith crack, the yield curve in stress-invariant space is given by

$$\frac{\left(2\sigma_I^i + P^i\right)^2}{\left(P^{*i}\right)^2} + \frac{\left(2e\sigma_{II}^i\right)^2}{\left(P^{*i}\right)^2} = 1, \tag{A1}$$

where P^i is the pressure in the ith crack, P^{*i} is the compressive strength of plastically deforming sea ice and is given by $P^{*i} = P^* h^i$, where $P^* \simeq 0.197 \times 10^6$ N/m^2 and the aspect ratio of major to minor axes of the elliptic yield curve is given by $e = \sqrt{1.91}$. The bulk and shear viscosities are given by

$$\zeta^i = \frac{P^{*i}}{2\Delta^i} \text{ and } \eta^i = \frac{\zeta^i}{e^2}, \tag{A2}$$

respectively, where

$$\Delta^i = \sqrt{\left(\dot{\epsilon}_I^i\right)^2 + \frac{\left(\dot{\epsilon}_{II}^i\right)^2}{e^2}}, \tag{A3}$$

and $\dot{\epsilon}_I^i$ and $\dot{\epsilon}_{II}^i$ are the first and second invariants of the strain-rate in the ith crack.

[70] The compressive ice strength in the ith crack P^{*i} is related to the pressure P^i, by

$$P^i = kP^{*i} = 2k\Delta^i\zeta \tag{A4}$$

[*Hibler and Schulson*, 2000], where k is a positive, real number less than unity.

[71] The value of the alternative strain-rate invariant in the ith crack $\theta^i = \tan^{-1}\left(\dot{\epsilon}_{II}^i / \dot{\epsilon}_I^i\right)$ for which $\sigma_I^i = 0$ can be straightforwardly calculated using (17) to be

$$\theta^i = \tan^{-1}\left(\frac{e\sqrt{1-k^2}}{k}\right). \tag{A5}$$

Since it was shown in section 2.2 that $|\theta^i| \geq \pi/4$, we set our value of k so that $\sigma_I^i = 0$ at $\theta^i = \pi/4$ (uniaxial extension across a crack) yielding $k = e/\sqrt{1+e^2} = 0.81$.

A2. Modified Coulombic Elliptic Yield Curve

[72] *Hibler and Schulson* [2000] introduced a modified elliptic yield curve that was mainly Coulombic (linear) under divergence and elliptic under convergence, and was based on biaxial compression experiments on brittle sea ice. The resulting yield curve is the shape of a full ice cream cone. The flow law is associated on the elliptic part of the yield curve but nonassociated (the strain-rate is not normal to the yield curve) in the Coulombic regime. To obtain the modified Coulombic elliptic yield curve, the shear viscosity of the elliptic yield curve (equation (A2)) is modified so that

$$\eta^i = \min\left(\frac{\zeta^i}{e^2}, \frac{1}{\beta\dot{\epsilon}_{II}^i}\left\{\frac{P^i}{\alpha} - \zeta^i\dot{\epsilon}_I^i\right\}\right), \tag{A6}$$

where α and β are constants that determine the gradient and position of the Coulombic section of the yield curve, which is given by

$$\sigma_{II}^i = -\frac{\sigma_I^i}{\beta} + \frac{P^i}{\beta}\left(\frac{1}{\alpha} - \frac{1}{2}\right). \tag{A7}$$

We follow *Hibler and Schulson* [2000] and take $\alpha = 1.8$ and $\beta = 1.4$.

A3. Linear Yield Curve

[73] We consider a linear material yield curve given simply by the Coulombic portion of *Hibler and Schulson*'s [2000] modified Coulombic elliptical yield curve so that the shear viscosity is given by

$$\eta^i = \frac{1}{\beta\dot{\epsilon}_{II}^i}\left\{\frac{P^i}{\alpha} - \zeta^i\dot{\epsilon}_I^i\right\}, \tag{A8}$$

with $\alpha = 1.8$ and $\beta = 1.4$ as above. The flow rule for this yield curve is nonassociated with the value of stress varying smoothly along the yield line from low to high values of $|\sigma_I|$ as θ^i varies from $\pi/4$ to π (uniaxial extension to pure convergence), where the minimum value of θ^i arises following the discussion in section 2.2.

References

Coon, M. D., G. A. Maykut, R. S. Pritchard, D. A. Rothrock, and A. S. Thorndike (1974), Modeling the pack ice as an elastic-plastic material, *AIDJEX Rep.*, *24*, 1–105.

Cox, G. F. N., and J. A. Richter-Menge (1984), Mechanical properties of multi-year sea ice triaxial tests, *Tech. Rep.*, U. S. Army Corps of Eng., Cold Reg. Res. and Eng. Lab.

Erlingsson, B. (1988), Two-dimensional deformation patterns in sea ice, *J. Glaciol.*, *34*(118), 301–308.

Feltham, D. L. (2005), Granular flow in the marginal ice zone, *Philos. Trans. R. Soc. A*, *363*, 1677–1700.

Feltham, D. L., P. R. Sammonds, and D. C. Hatton (2002), Method of determining a geophysical-scale sea ice rheology from laboratory experiments, in *Proceedings of the 16th IAHR Symposium on Ice.*

Gray, J. M. N. T., and L. W. Morland (1994), A two-dimensional model for the dynamics of sea ice, *Philos. Trans. R. Soc. A*, *347*, 219–290.

Hibler, W. D., III (1979), A dynamic thermodynamic sea ice model, *J. Phys. Oceanogr.*, *9*, 819–845.

Hibler, W. D., III, and E. M. Schulson (2000), On modeling the anisotropic failure and flow of flawed sea ice, *J. Geophys. Res.*, *105*(C7), 17,105–17,120.

Hopkins, M. A. (1996), On the mesoscale interaction of lead ice and floes, *J. Geophys. Res.*, *101*, 18,315–18,326.

Marko, J. R., and R. Thomson (1977), Rectilinear leads and internal motions in the ice pack of the western arctic ocean, *J. Geophys. Res.*, *82*(C6), 979–987.

Miller, P. A., S. W. Laxon, D. L. Feltham, and D. J. Cresswell (2006), Optimization of a sea ice model using basin-wide observations of arctic sea ice thickness, extent and velocity, *J. Clim.*, *19*, 1089–1108.

Moritz, R. E., and J. Ukita (2000), Geometry and the deformation of pack ice: I. a simple kinematic model, *Ann. Glaciol.*, *31*, 313–322.

Overland, J. E., B. A. Walter, T. B. Curtin, and P. Turet (1995), Hierarchy and sea ice mechanics: A case study from the Beaufort Sea, *J. Geophys. Res.*, *100*, 4559–4571.

Sammonds, P. R., D. C. Hatton, D. L. Feltham, and P. D. Taylor (2005), Experimental study of sliding friction and stick-slip on faults in floating ice sheets, in *Proceedings of the 18th International Conference on Port and Ocean Engineering Under Arctic Conditions (POAC)*.

Shen, H. H., W. D. Hibler III, and M. Leppäranta (1987), The role of floe collisions in sea ice rheology, *J. Geophys. Res.*, *92*, 7085–7096.

Thorndike, A. S. (1987), A random discontinuous model of sea ice motion, *J. Geophys. Res.*, *92*(C6), 6515–6520.

Tremblay, L. B., and L. A. Mysak (1997), Modelling sea ice as a granular material, including the dilatancy effect, *J. Phys. Oceanogr.*, *27*, 2342–2360.

Ukita, J., and R. E. Moritz (2000), Geometry and the deformation of pack ice: II. simulation with a random isotropic model and implication in sea-ice rheology, *Ann. Glaciol.*, *31*, 323–326.

Weeks, W. F. (1983), The variation of ice strength within and between multi-year pressure ridges in the Beaufort Sea, paper presented at Third International Symposium on Offshore Mechanics and Arctic Engineering, New Orleans, La., 12–17 Feb.

Wilchinsky, A. V., and D. L. Feltham (2004a), Dependence of sea ice yield curve shape on ice thickness, *J. Phys. Oceanogr.*, *34*(12), 2852–2856.

Wilchinsky, A. V., and D. L. Feltham (2004b), A continuum anisotropic model of sea ice dynamics, *Proc. R. Soc. A*, *460*(2), 2105–2140.

Wilchinsky, A. V., and D. L. Feltham (2006a), Anisotropic model for granulated sea ice dynamics, *J. Mech. Phys. Solids*, *54*(6), 1147–1185.

Wilchinsky, A. V., and D. L. Feltham (2006b), Modelling the rheology of sea ice as a collection of diamond-shaped floes, *J. Non-Newtonian Fluid Mech*, *138*, 22–32.

Wilchinsky, A. V., D. L. Feltham, and P. A. Miller (2006), A multi-thickness sea ice model accounting for sliding friction, *J. Phys. Oceanogr*, *36*, 1719–1737.

D. L. Feltham and P. D. Taylor, Centre for Polar Observation and Modelling, Department of Earth Sciences, University College London, Gower Street, London WC1E 6BT, UK. (dlf@cpom.ucl.ac.uk)

D. Hatton and P. R. Sammonds, Mineral, Ice and Rock Physics Laboratory and Centre for Polar Observation and Modelling, Department of Earth Sciences, University College London, Gower Street, London WC1E 6BT, UK.